RSC Advances

PAPER

View Article Online
View Journal | View Issue

Cite this: *RSC Adv.*, 2025, **15**, 19079

Single-metal atoms supported on HfBO MBenes for efficient overall water splitting†

Meiling Pan,[a] Xiuhua Cui,*[a] Qun Jing,[ab] Haiming Duan,*[a] Fangping Ouyang*[ab] and Rong Wu[a]

Received 3rd April 2025
Accepted 11th May 2025

DOI: 10.1039/d5ra02327k

rsc.li/rsc-advances

Two-dimensional hexagonal MBenes (h-MBenes), derived from h-MAB phases, exhibit great potential for electrochemical applications due to their unique electronic and catalytic properties. Using first-principles calculations, we explored single-atom transition metals (TMs) supported on h-MBene HfBO (TM@HfBO) as bifunctional catalysts for the hydrogen evolution reaction (HER) and oxygen evolution reaction (OER). TM@HfBO structures demonstrated excellent thermal stability and high electrical conductivity, making them suitable for electrocatalysis. For HER, Nb@HfBO showed outstanding activity with a near-ideal hydrogen adsorption free energy ($\Delta G_H = -0.01$ eV), surpassing even platinum. For OER, ferromagnetic TM@HfBO systems (TM = Fe, Co, Ni) exhibited high catalytic potential, with Ni@HfBO achieving the lowest overpotential ($\eta_{OER} = 0.48$ V), outperforming IrO_2 ($\eta_{OER} = 0.56$ V). These results highlight TM@HfBO as a promising alternative to noble-metal-based catalysts. Our findings provide a foundation for designing cost-effective, high-performance electrocatalysts for overall water splitting and underscore the potential of HfBO-based materials in sustainable energy applications.

1 Introduction

The search for clean and sustainable energy sources is a major challenge but is crucial to address the issues around the scarcity of fossil fuel resources and the increasing environmental pollution.[1,2] Electrochemical water splitting using renewable electricity is an efficient method to produce high-purity hydrogen. Water electrolysis consists of two half reactions: the hydrogen evolution reaction (HER) and oxygen evolution reaction (OER).[3–5,31–34] The kinetics of these electrochemical reactions are slow, resulting in a high water-splitting overpotential. In addition, the high cost of using precious metals (platinum, ruthenium, and iridium) as electrode materials for water splitting has limited the widespread commercialization of water electrolysis.[6] Nowadays, the efficiency and stability of catalysts are the key factors restricting the widespread application of water splitting.

Two-dimensional (2D) electrocatalysts, such as transition metal carbides/nitrides (MXenes),[7,8] g-C_3N_4, and sulfides,[9,10] have received increasing attention owing to their high specific surface area and unique electronic structure. In particular, 2D transition metal borides, known as MBenes, have been extensively studied. For example, FeB_2,[11] MoB_2,[12] and TiB_2 (ref. 13) are expected to be excellent alternatives for metal-ion batteries, magnetic devices, and, especially, electrocatalysts. MBenes are known to have an abundance of ligand-unsaturated active sites, which facilitate charge and mass transfer in catalytic processes. In addition, MBenes are an ideal matrix for supporting single-atom catalysts.

In 2019, Wang's group successfully synthesized[14] the first ternary hexagonal phase MAB (h-MAB) of Ti_2InB_2, wherein the indium layer could be experimentally removed to form layered TiB. Notably, h-MBs, the derivatives of h-M_2AB_2, can be formed as diverse stable compounds, including 2D TiB, CrB, MoB, and WB, according to theoretical calculations. These bare h-MBs may be promising electrochemical nitrogen reduction reaction (eNRR) electrocatalysts based on calculations of their Gibbs free energy. Furthermore, Feng and co-workers systematically investigated the effect of transition metal doping on the HER electrocatalytic activity of the h-MBene Hf_2BO_2 using first-principles calculations and finally screened out V@Hf_2BO_2 and Cr@Hf_2BO_2, suggesting that they would exhibit excellent HER electrocatalytic activity.[15–17] In 2023, Wang's group found, through theoretical calculations, that ternary h-MAB was more suitable as a precursor for MBenes than the orthorhombic symmetric phase (*ortho*-MAB), and succeeded in synthesizing h-MBene HfBO by the selective removal of In from h-MAB Hf_2InB_2, which demonstrated good metallic electrical conductivity and excellent cyclic stability for lithium storage.[18] Therefore, we expect that HfBO would exhibit excellent

---

[a] *Xinjiang Key Laboratory of Solid State Physics and Devices, School of Physical Science and Technology, Xinjiang University, 777 Huarui Street, Urumqi 830017, China. E-mail: xjcxh0991@xju.edu.cn; dhm@xju.edu.cn*

[b] *School of Physics, Hunan Key Laboratory for Super-Microstructure and Ultrafast Process, Hunan Key Laboratory of Nanophotonics and Devices, Central South University, Changsha 410083, China. E-mail: oyfp@csu.edu.cn*

† Electronic supplementary information (ESI) available. See DOI: **https://doi.org/10.1039/d5ra02327k**

electrocatalytic properties. To the best of our knowledge, water splitting by HfBO has not been reported to date, either theoretically or experimentally.

In this work, we designed a series of transition metal catalysts anchored to HfBO and systematically investigated their catalytic activities for the HER and OER by density functional theory (DFT) calculations. Efficient electrolytic catalysts for water electrolysis were found by establishing volcano-type activity maps for the HER and OER. In particular, Nb@HfBO was found to have excellent catalytic activity for the HER. Ni@HfBO could also be expected to be a promising candidate as a highly active OER electrocatalyst. The intrinsic descriptor φ involving the d-orbital electron number and electronegativity of TM was applied to predict the ORR activity. This allowed predicting and revealing the origin of the OER activity, which provides a cost-effective solution for the rapid screening of highly efficient bifunctional catalysts based on TM@HfBO.

2 Computational methods

Herein, all the spin-polarized density functional theory (DFT) calculations were conducted using the Vienna *ab initio* Simulation Package (VASP).[19,20] The projector-augmented wave method was employed with a cut-off energy of 500 eV.[21] The Perdew–Burke–Ernzerhof (PBE) functional was adopted under the generalized gradient approximation (GGA) to treat the electronic exchange–correlation interactions.[22] The total energy and force convergence tolerances adopted for the calculations used in this study were 10^{-5} eV and 0.02 eV Å^{-1}. The HfBO ($3 \times 3 \times 1$) monolayer supercell was adopted with a vacuum layer of 15 Å, for which Brillouin zones were sampled with $2 \times 2 \times 1$ and $4 \times 4 \times 1$ Monkhorst–Pack meshes for geometry optimization and for the electronic structure calculations, respectively. Dispersion corrections in Grimme's scheme (DFT-D3) were applied to describe the van der Waals interactions.[23] The climbing image nudged elastic band (CI-NEB) method was adopted to determine the diffusion energy barriers for the transition metal atoms of neighboring sites[24] and *ab initio* molecular dynamics (AIMD) simulations were performed in the NVT ensemble to examine the thermodynamic stability of the TM@HfBO systems.[25] The adsorption energy (E_{ads}) for the TM single-atom on the HfBO monolayer was studied using the following equation:

$$E_{\text{ads}} = E_{\text{TM@HfBO}} - E_{\text{HfBO}} - E_{\text{TM}} \tag{1}$$

where $E_{\text{TM@HfBO}}$, E_{HfBO}, and E_{TM} are the total energies of the TM@HfBO monolayer, bare HfBO, and isolated TM atom, respectively.

The energy of the ($H^+ + e^-$) pair could be substituted by half of a H_2 molecule.[26] To avoid calculating the free energy of O_2 gas, the experimental reaction energy of $2H_2O \rightarrow O_2 + 2H_2$ (4.92 eV) was used. Based on each individual step, the free energy change for the four elementary OER steps can be expressed as follows:

$$\Delta G_1 = \Delta G_{\text{OH*}} \tag{2}$$

$$\Delta G_2 = \Delta G_{\text{O*}} - \Delta G_{\text{OH*}} \tag{3}$$

$$\Delta G_3 = \Delta G_{\text{OOH*}} - \Delta G_{\text{O*}} \tag{4}$$

$$\Delta G_4 = 4.92 - \Delta G_{\text{OOH*}} \tag{5}$$

where $\Delta G_{\text{OH*}}$, $\Delta G_{\text{O*}}$, and $\Delta G_{\text{OOH*}}$ are the binding free energies of OH*, O*, OOH*, which are expressed as:

$$\Delta G_{\text{O*}} = G_{\text{O*}} - G_* - (G_{H_2O} - G_{H_2}) \tag{6}$$

$$\Delta G_{\text{OH*}} = G_{\text{OH}} - G_* - (G_{H_2O} - 1/2G_{H_2}) \tag{7}$$

$$\Delta G_{\text{OOH*}} = G_{\text{OOH*}} - G_* - (2G_{H_2O} - 3/2G_{H_2}) \tag{8}$$

where G_*, $G_{\text{OH*}}$, $G_{\text{O*}}$, and $G_{\text{OOH*}}$ are the free energies of *, OH*, O*, and OOH*, respectively. The Gibbs free energy (G) can be determined as follows:

$$\Delta G = \Delta E + \Delta E_{\text{ZPE}} - T\Delta S_{\text{H}} \tag{9}$$

where ΔE is the adsorption energy of atomic hydrogen, ΔE_{ZPE} is the zero-point energy difference between the adsorbed-state and gas-phase hydrogen, ΔS_{H} is the entropy contribution of atomic hydrogen adsorption, and T is room temperature (298 K).

We obtained the theoretical exchange current density (i_0) at pH 0 based on Norskov's assumption,[26] which can be can defined as:

$$i_0 = -ek_0 \frac{1}{1 + \exp(|\Delta G_{\text{H}}|/k_{\text{B}}T)} \tag{10}$$

where k_{B} and k_0 are the Boltzmann constant and rate constant, respectively. Herein, k_0 was set to 1.[27] The difference between the electrode potential and equilibrium potential is defined as the theoretical overpotential (η), which can be calculated using the following formula:

$$\eta_{\text{HER}}\ (\text{mV}) = -|\Delta G_{\text{H}}|/e \times 10^3 \tag{11}$$

3 Results and discussion

3.1 Structure and stability of TM@HfBO

The optimized HfBO possessed a hexagonal lattice with $a = b = 3.124$ Å (Fig. 1a), which was in good agreement with the previous results.[28] The PBE band structure and projected density of states (PDOS) diagrams in Fig. 1b show that the pure HfBO monolayer (ML) had a band gap value of 0 V, with the main contributions at the Fermi energy level being from the Hf-5d and O-2p orbitals. To design efficient single-atom catalysts for water electrolysis, we explored the catalytic properties of 19 TMs (TM = V, Cr, Mn, Fe, Co, Ni, Cu, Vb, Mo, Ru, Rh, Pd, Ag, Ta, W, Os, Ir, Pt, Au) anchored on pure HfBO ML (TM@HfBO). The adsorption configurations and adsorption energies were investigated to determine the stability of the TM@HfBO systems. Generally, the TM atoms had two distinct adsorption sites: the hollow Hf site (blue circle) and the hollow B site (orange circle), as shown in Fig. 1a. The results are illustrated in

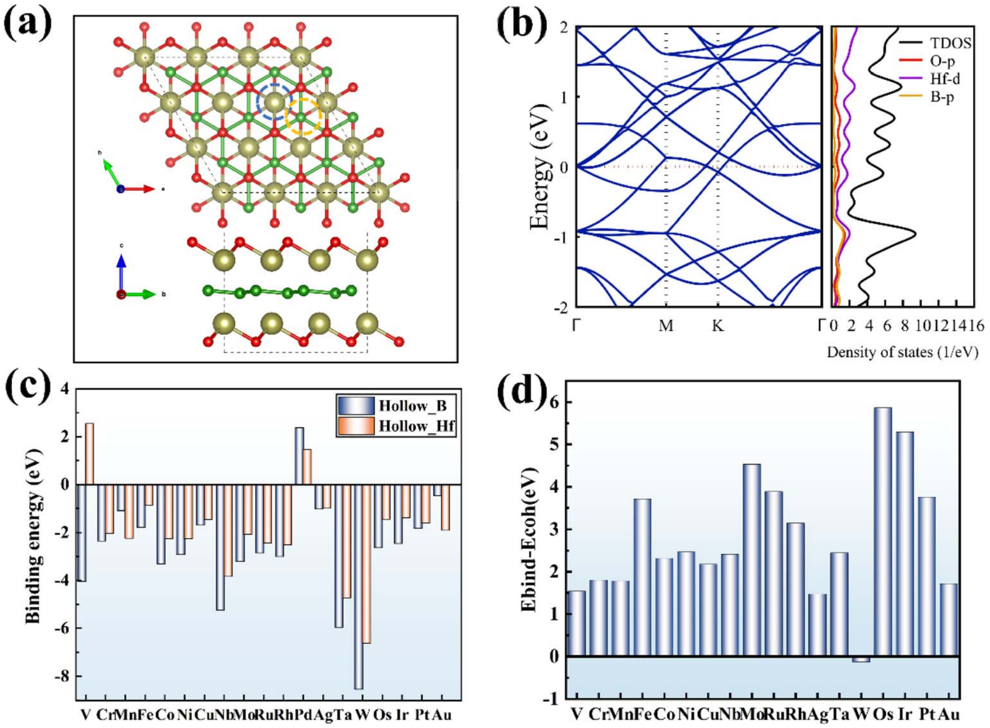

Fig. 1 (a) Top and side views of the original HfBO monolayer and the adsorption sites (Hollow_B and Hollow_Hf) of various TM monoatoms. (b) Band structure and density of states of HfBO calculated using the PBE function. (c) Binding energies (E_{bind} in eV) of various TM monoatoms on the HfBO ML. (d) Comparison of the corresponding cluster energies.

Fig. 1c, where the binding energy on the hollow H_f site and hollow B sites are indicated by blue and orange bar graphs, respectively. It could be observed that the adsorption energies of all the TM atoms on the hollow H_f and hollow O sites were negative (except for V and Pd atoms), implying that the adsorption of TM atoms on the HfBO surface was thermodynamically favorable. In terms of the adsorption configurations, all the TM atoms preferred to adsorb on the hollow B site, except for Au and Pd, which preferred to adsorb on the hollow Hf site.

In order to examine the aggregation possibility of TM@HfBO ML, *i.e.*, the thermodynamic stability, we calculated the cluster energies of TM@HfBO ($\Delta E_{\text{clus}} = \Delta E_{\text{bind}} - \Delta E_{\text{coh}}$), where ΔE_{bind} and ΔE_{coh} are the binding and cohesion energies of the TM atoms, respectively. The binding energies (ΔE_{bind}) of the metal atoms on HfBO, and the TM bulk cohesive energy (ΔE_{coh}) are defined as $\Delta E_{\text{bind}} = E_{\text{TM/HfBO}} - E_{\text{HfBO}} - E_{\text{TM-single}}$, and $\Delta E_{\text{coh}} = E_{\text{TM-bulk/N}} - E_{\text{TM-single}}$, where $E_{\text{TM/HfBO}}$, E_{HfBO}, $E_{\text{TM-single}}$ and $E_{\text{TM-bulk}}$ are the total energies of the HfBO (with and without TM) and TM (vacuum and bulk), respectively. According to Fig. 1d, the calculations indicated that $E_{\text{clus}} > 0$ for all the structures, except for W@HfBO, suggesting that these TM atoms were likely to aggregate. However, even with a positive E_{clus} value, the TM atoms were stable on the substrate when the diffusion energy barrier (E_{barrier}) was high enough to prevent aggregation, which was attributed to the kinetic stability of the SAC.[29] Therefore, we subsequently calculated the E_{barrier} for the migration of the TM to sub-stable sites for TM@HfBO with $E_{\text{clus}} > 0$, as shown in Fig. 2a, wherein the results indicated that the diffusion barriers for all the TM atoms, except Cu, Ag, Pt, and Au atoms, were greater than 1.00 eV, which suggests that the TM atoms did not have the potential to drift and aggregate into clusters. Finally, we excluded the unstable structures, *i.e.*, Pd, Cu, Ag, Pt, and Au atoms, and investigated the catalytic properties of the remaining 14 stable structures.

The thermal stability of TM@HfBO was further evaluated by AIMD simulation, as shown in Fig. 3. The results show that the TM@HfBO monolayer had good kinetic and thermodynamic stability at 300 K.

3.2 Hydrogen evolution reaction activity

We first investigated the hydrogen reactivity of the TM@HfBO systems using the hydrogen adsorption free energy (ΔG_{H^*}). Generally, the closer ΔG_{H} is to zero, the higher the hydrogen reactivity of TM@HfBO. The calculation results are shown in Fig. 4a, in which for the studied TM@HfBO systems, the catalytic HER activity was superior to that of pristine HfBO ($\Delta G_{\text{H}^*} = 0.42$ V) for Nb@HfBO, W@HfBO, Mo@HfBO, V@HfBO, Fe@HfBO, Ir@HfBO, Co@HfBO, and Mn@HfBO, which corresponded to ΔG_{H^*} values of −0.01, −0.02, −0.02, −0.26, −0.30, 0.32, 0.33, and 0.33 eV, respectively. In particular, the ΔG_{H^*} value of Nb@HfBO was −0.01 eV, which was even better than that of the Pt-based catalyst (−0.09 eV). For the remaining TM atoms, the results imply that the O atoms of Ir@HfBO, V@HfBO, and Fe@HfBO could act as the active sites for an efficient HER. The adsorption properties of H on the O atoms of M@HfBO were also investigated, as shown in Fig. S1.† Except

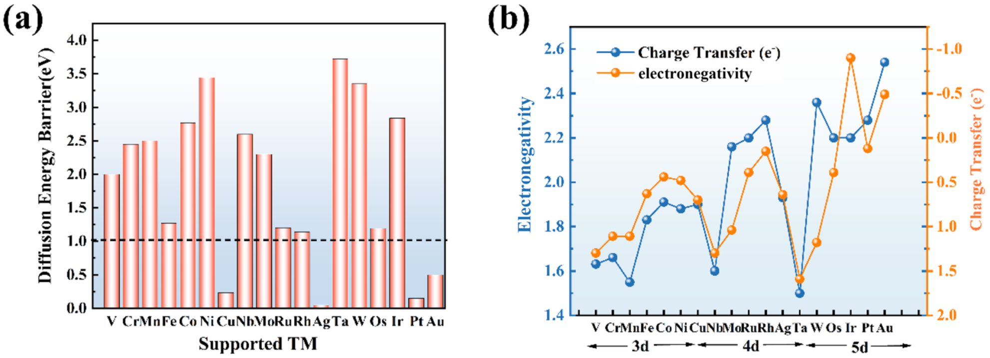

Fig. 2 (a) Diffusion barriers of TM@HfBO. (b) Charge transfer (blue) and electronegativity (yellow) of TM atoms.

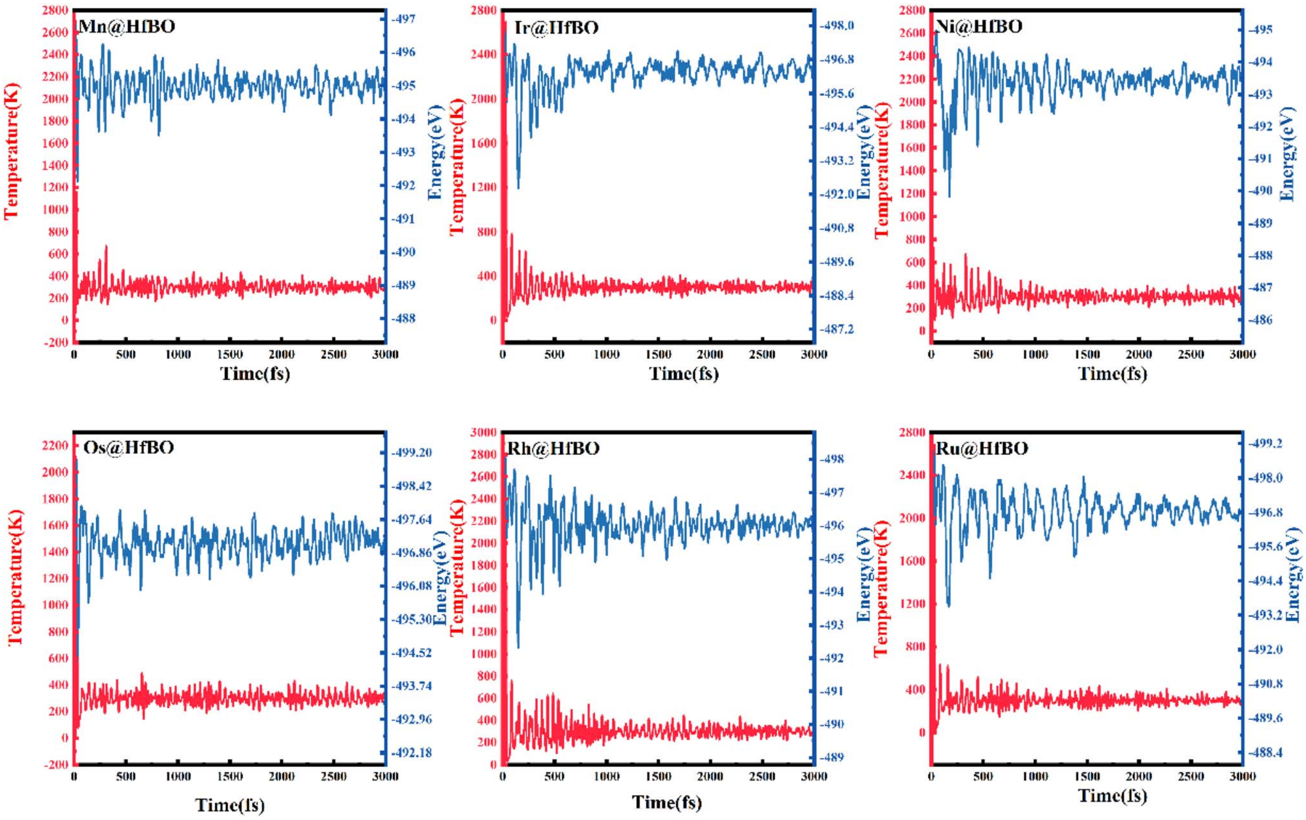

Fig. 3 Temperature and energy variations of TM@HfBO in 3000 fs AIMD simulations at a temperature of 300 K.

for Ir@HfBO ($\Delta G_{H^*} = -0.05$ eV), Ru@HfBO ($\Delta G_{H^*} = 0.11$ eV), and Os@HfBO ($\Delta G_{H^*} = 0.35$ eV), all the other systems had $|\Delta G_{H^*}|$ values in the range of 0.55–0.72 eV, which were larger than those of H on the TM atoms (Fig. 4a). It was noteworthy that H preferred to adsorb on the TM atoms, and thus the TM atoms were identified as the active sites. Fig. 4b displays the volcanic curves drawn according to the theoretical exchange current density (i_0) and overpotential (η). In general, the best HER catalysts located near the peak of the volcano curve usually have the highest i_0 and lower η_{HER}. Notably, TM@HfBO (TM = Nb, W, Mn, Ir) were closer to the peak of the volcano and exhibited superior HER activity, outperforming the state-of-the-art Pt catalyst (−0.09 eV).[30]

The HER process consists of two reaction steps: H adsorption and H_2 formation. In order to gain a deeper understanding of the HER kinetic mechanism of the Nb@HfBO catalyst, we further investigated the second step (H_2 formation), as shown in Fig. 5. The HER formation of H_2 has been reported to mainly occur through Heyrovsky mechanism ($H^* + H^+ + e^- \rightarrow H_2 + *$) or Tafel reaction ($H^* + H^* \rightarrow H_2 + *$). The results herein showed that the kinetic potential for the Heyrovsky reaction of Nb@HfBO (0.89 eV) was much lower than that of the Tafel

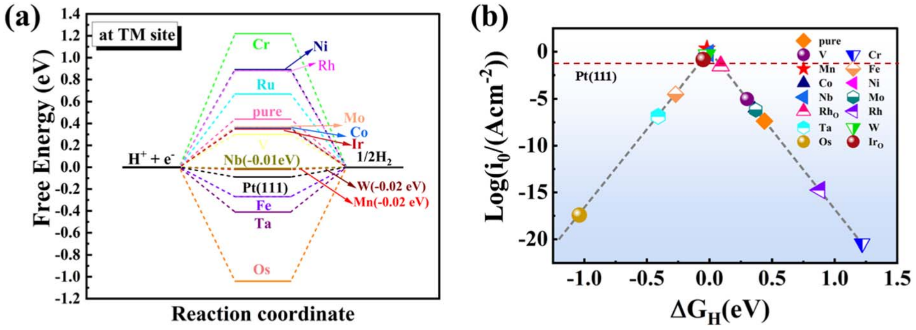

Fig. 4 (a) Gibbs free energy diagram of the HER on the TM atoms of the TM@HfBO catalyst. (b) HER volcano profile for HfBO catalyst exchange current (i_0).

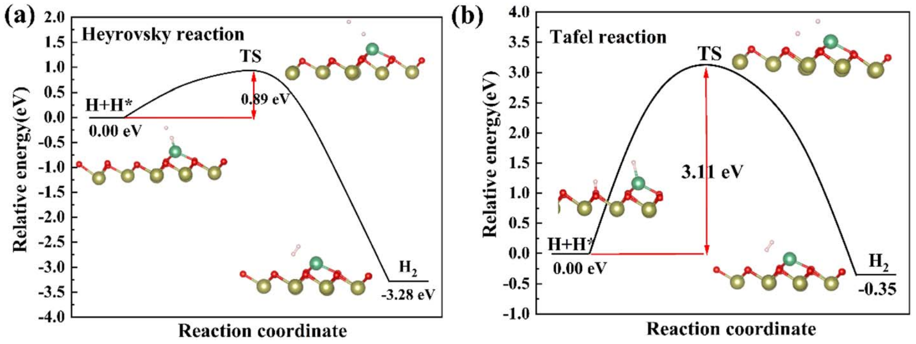

Fig. 5 (a) Heyrovsky reaction and (b) Tafel reaction of the HER on Nb@HfBO.

reaction (3.11 eV). Therefore, Nb@HfBO preferred the Tafel reaction to the Heyrovsky reaction.

3.3 OER catalytic activity

For the OER, we calculated the Gibbs free energy change for each of the basic reactions of the TM@HfBO systems, as shown in Fig. 6 and S2.† From the free energy plots, it could be seen that for V@HfBO, Ir@HfBO, Nb@HfBO, Mo@HfBO, Ta@HfBO, W@HfBO, Rh@HfBO, Co@HfBO, Cr@HfBO, Os@HfBO and Ru@HfBO, Mn@HfBO the fourth step in the formation of O_2 from the OOH* species was the potential determining step (PDS) in the whole OER, with ΔG_4 values of 5.64, 6.85, 4.38, 8.08, 6.66, 8.64, 7.70, 1.80, 1.79, 4.28, 3.07, 3.17, 3.31 eV, respectively, and the poor performance of these catalysts was attributed to the fact that the adsorption energy of the OOH intermediate OOH* was too strong for the desorption of O_2. For Ni@HfBO and Fe@HfBO, OOH* formation was identified as the PDS of the OER process, with ΔG_3 values of 1.71 and 1.99 eV, respectively. In addition, we calculated the overpotential of TM@HfBO, which is the most important factor in determining the OER performance. The overpotential of the OER process is determined by the PDS. The results showed that Ni@HfBO had the lowest overpotential ($\eta_{\mathrm{OER}} = 0.48$ V), which was significantly lower than that of pristine HfBO ($\eta_{\mathrm{OER}} = 0.78$ V), and even better than the catalytic activity of the state-of-the-art IrO_2 ($\eta_{\mathrm{OER}} \sim 0.56$ eV). In addition, the η_{OER} of Rh@HfBO and Fe@HfBO were 0.48 and 0.76 V, respectively, and the corresponding PDSs were OOH* species forming O_2 and OOH* species forming O_2, respectively. The other TM@HfBO systems had larger η_{OER} values (3.05–3.31 V), and the PDSs were the OOH* species forming O_2, respectively. Except for Ni@HfBO, Co@HfBO also showed a relatively low OER overpotential of 0.56 V, which suggests its good catalytic performance for the OER.

In previous studies, the Gibbs free energies of the three intermediates (ΔG_{OH^*}, ΔG_{O^*}, and $\Delta G_{\mathrm{OOH}^*}$) were considered as possible descriptors of the strength of binding between the active atoms of the catalyst and the intermediates. If there is a simple linear relationship between the adsorption strengths of these reaction intermediates, the descriptor-based approach can greatly reduce the evaluation of complex OER/ORR catalytic activities. Previous studies have shown that similar TM–O bonding between TMs and the intermediates (OH*, O*, OOH*) may lead to similar trends in the adsorption energies of the oxygenated intermediates on the catalysts.[29,30] Moreover, the Gibbs free energy diagram above shows that most of the TM@HfBO systems had excess adsorption energy for OOH*, leading to the PDS being the last step, so we explored the relationship between ΔG_{OH^*} and $\Delta G_{\mathrm{OOH}^*}$. As shown in Fig. 7a, ΔG_{OH^*} and $\Delta G_{\mathrm{OOH}^*}$ showed a high linear correlation, which could be described by the following expression: $\Delta G_{\mathrm{OOH}^*} = \Delta G_{\mathrm{OH}^*} + 0.74$ eV, with a coefficient of determination (R^2) of 0.972. Volcano plots are widely considered to be a powerful guide for the selection of efficient catalysts. According to the scaling relationship, a volcano plot for the OER overpotential

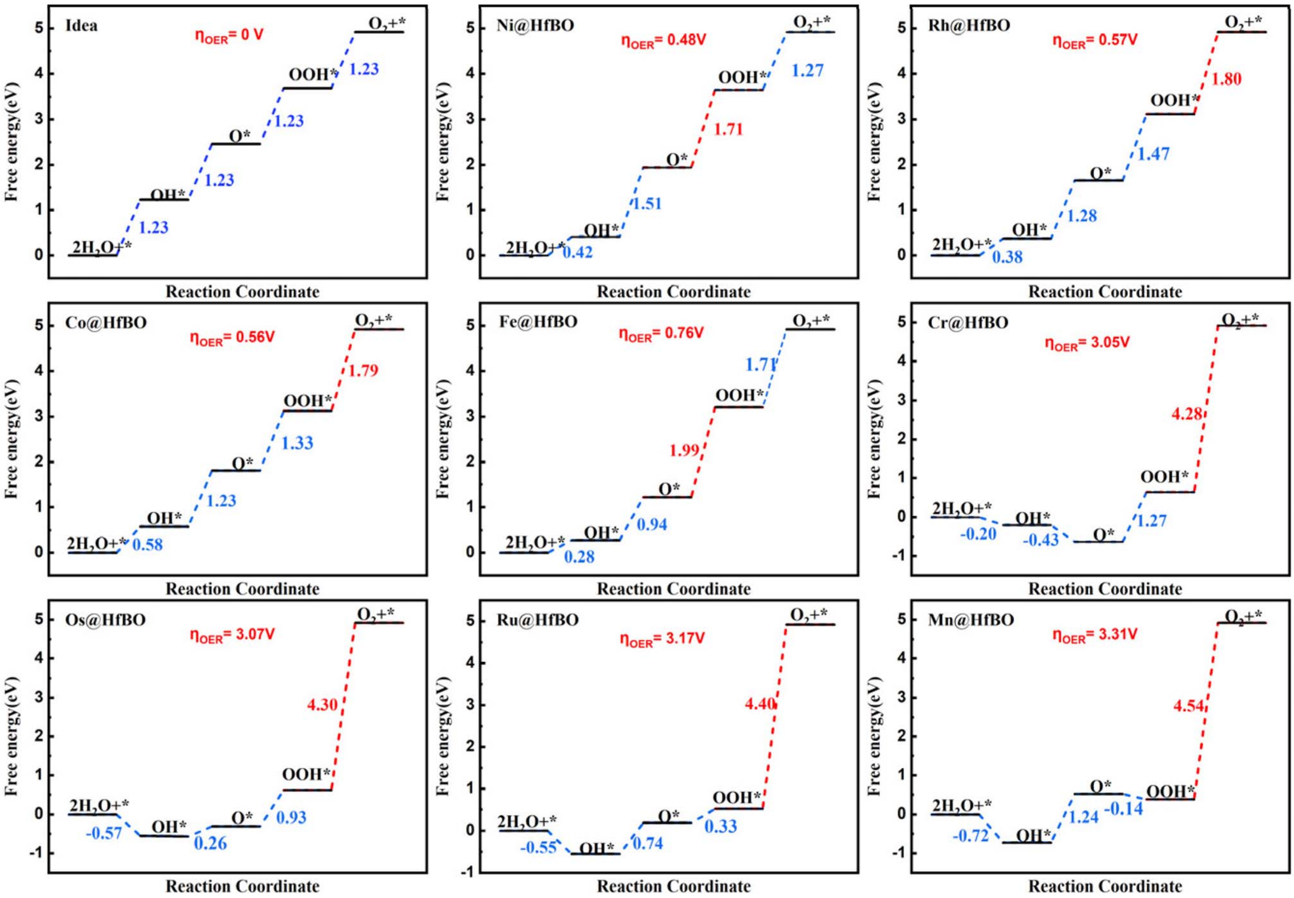

Fig. 6 Gibbs free energy diagram of the OER over the TM@HfBO catalyst at zero potential ($U = 0$).

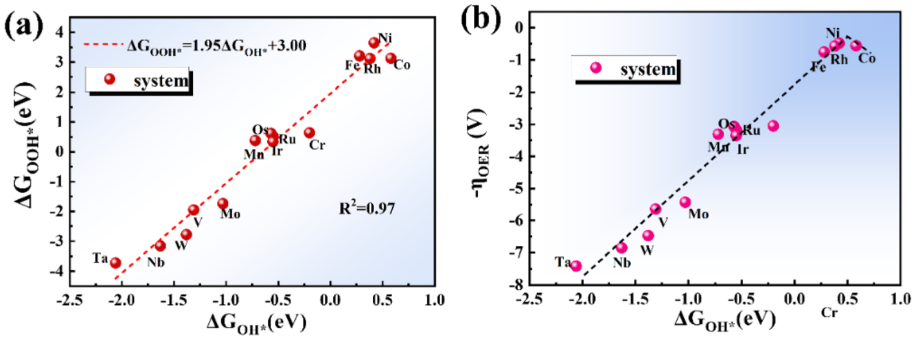

Fig. 7 (a) Linear relationship between ΔG_{OH*} and ΔG_{OOH*} of the HfBO catalytic systems. (b) Volcano plot for the OER for TM@HfBO.

(η_{OER}) was constructed, as shown in Fig. 7b, which was described by ΔG_{OH*}. On the left side of the volcano plot, it can be seen that the catalytic activity of the OER gradually increased with the increase in ΔG_{OH*}, and when ΔG_{OH*} reached 0.48 eV, the catalytic activity of the OER is the highest. On the right side of the volcano plot, it can be seen that the catalytic activity of the OER gradually decreased with the increase in ΔG_{OH*}, Obviously, in the studied TM@HfBO systems, Ni@HfBO was located at the top of the OER volcanic map, with the lowest overpotential of 0.48 eV, followed by Co@HfBO (0.56 eV) and Fe@HfBO (0.76 eV). In summary, the ferromagnetic system TM@HfBO (TM = Ni, Fe, Co) would be highly promising as electrocatalysts for the OER. In particular, the catalytic activity of Ni@HfBO for the OER was even lower than that of the state-of-the-art IrO_2 ($\eta_{OER} \sim$ 0.56 eV).

For SACs, the interaction between the metal and substrate is a significant factor affecting the catalytic activity of the catalysts. This is because anchoring a metal atom will cause charge redistribution. Thus, we calculated the charge transfer for all the TM@HfBO candidates. As shown in Fig. 2b, Bader charge

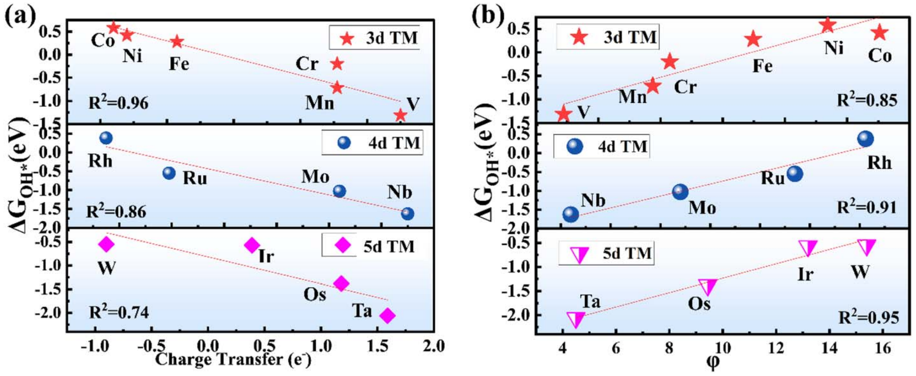

Fig. 8 (a) Charge transfer *versus* ΔG_{OH^*} and (b) φ *versus* ΔG_{OH^*}.

analysis was carried out to understand the valence states of the TM atom, wherein charge transfer from the TM atom to HfBO left the TM atom positively charged, indicating a strong interaction between the TM atom and HfBO. In each cycle, the amount of charge transfer decreased from left to right, which was in good agreement with the electronegativity trend. Ta demonstrated a charge transfer of 1.55e with a lowest electronegativity of 1.50, while Au had a reduced charge transfer of 0.47e and an electronegativity of 2.40. Furthermore, the positive charges on the TM atoms are particularly suited to adsorbing OER intermediates, which can effectively promote the OER.

In order to better understand the significant differences in the OER catalytic activity of the various catalysts, we further explored the possibility of using the charge transfer of the TM as a descriptor to predict the OER activity. From the above, it is clear that ΔG_{OH^*} can describe the OER activity of a material alone, so we first explored the relationship between the Bader charge transfer of the TM and the OH adsorption energy. As shown in Fig. 8a, there was a clear linear relationship between the charge transfer and the ΔG_{OH^*} adsorption energy of the TMs (3d $\sim$ 5d), indicating that the larger the charge of the TM atoms, the stronger the adsorption of the OH intermediates, and thus the worse the OER activity. *V*, with the most positive charge of 1.75e, showed the largest ΔG_{OH^*} of 1.48 eV among the 4d metals, while Co lost 0.82e with a ΔG_{OH^*} of 0.51 eV. The relationship between the charge transfer of the TMs and the oxygen–hydrogen (OH) adsorption energy was linear, with a high correlation coefficient. This indicates that an increased positive charge on the TM atom would result in a stronger adsorption of the oxygen reduction reaction (ORR) intermediates.

Through the above, we found that the amount of charge transfer of the TM affects the catalytic OER activity of TM@HfBO, therefore, we propose the descriptor (φ) to predict the OER activities of the TM@HfBO system considering the number of electrons in the d orbital (θ_d) and the electronegativity of the TM atoms (E_{TM}) as determined by the following equation:

$$\varphi = \theta_d \cdot E_{TM} \tag{12}$$

As shown in Fig. 8b, the linear relationship between the multiplication and ΔG_{OH^*} was quite good ($R^2 > 0.85$). This shows that the adsorption strength of OH and other intermediates can be easily determined by basic characterization, which provides a cost-effective solution for the rapid screening of efficient bifunctional catalysts based on TM@HfBO.

4 Conclusion

We systematically investigated 19 potential TM-doped HfBO catalysts as HER and OER electrochemical catalysts by first-principle calculations. All the TM@HfBO catalysts had excellent thermal stability due to their large binding and agglomeration energies. In particular, Nb@HfBO exhibited remarkable catalytic activity in the hydrogen evolution reaction with a ΔG_{H^*} value of -0.01 eV, which even exceeded the performance of platinum (Pt), while Ni@HfBO showed the highest activity in the OER with an overpotential (η_{OER}) of 0.48 V, which was even better than that of IrO_2 ($\eta_{OER} = 0.56$ V). In addition, based on the proportionality between the adsorption energies of the OER intermediates, we propose that ΔG_{OH^*} can be used as an energy descriptor to reflect the OER activity of the TM@HfBO system. In addition, the product of the number of electrons on the d orbitals and the electronegativity of TM atoms was used as a descriptor (φ) to predict the OER performance of TM@HfBO catalysts. In summary, this study provides a promising approach for the screening and use of high-performance catalysts based on HfBO for the electrolysis of water.

Data availability

All data included in this study are available upon request to the corresponding author.

Conflicts of interest

The authors declare that they have no known competing financial interests or personal relationships that could have appeared to influence the work reported in this paper.

Acknowledgements

This work has been supported by the National Natural Science Foundation of China (Grant No. 52073308), the Tianshan Talent

Training Program of Xinjiang Uygur Autonomous Region of China (2022TSYCJU0004), the Key Project of the Natural Science Program of Xinjiang Uygur Autonomous Region (Grant No. 2023D01D03). This work was also supported by the State Key Laboratory of Powder Metallurgy, Central South University, Changsha, China. Warm congratulations to Xinjiang University on its centennial anniversary.

References

1 J. M. Serra, J. F. Borrás-Morell, B. García-Baños, *et al.*, Hydrogen production *via* microwave-induced water splitting at low temperature, *Nat. Energy*, 2020, **5**(11), 910–919.

2 M. A. Mac Kinnon, J. Brouwer and S. Samuelsen, The role of natural gas and its infrastructure in mitigating greenhouse gas emissions, improving regional air quality, and renewable resource integration, *Prog. Energy Combust. Sci.*, 2018, **64**, 62–92.

3 J. Zhu, L. Hu, P. Zhao, *et al.*, Recent advances in electrocatalytic hydrogen evolution using nanoparticles, *Chem. Rev.*, 2019, **120**(2), 851–918.

4 F. M. Sapountzi, J. M. Gracia, H. O. A. Fredriksson, *et al.*, Electrocatalysts for the generation of hydrogen, oxygen and synthesis gas, *Prog. Energy Combust. Sci.*, 2017, **58**, 1–35.

5 K. Zeng and D. Zhang, Recent progress in alkaline water electrolysis for hydrogen production and applications, *Prog. Energy Combust. Sci.*, 2010, **36**(3), 307–326.

6 N. K. Chaudhari and B. Kim, Nanostructured materials on 3D nickel foam as electrocatalysts for water splitting, *Nanoscale*, 2017, **9**(34), 12231–12247.

7 B. Ding, W. J. Ong, J. Jiang, *et al.*, Uncovering the Electrochemical Mechanisms for Hydrogen Evolution Reaction of Heteroatom Doped M_2C MXene (M = Ti, Mo), *Appl. Surf. Sci.*, 2020, **500**(12), 143987.

8 Q. Yu, Y. Luo, S. Qiu, *et al.*, Tuning the Hydrogen Evolution Performance of Metallic 2D Tantalum Disulfide by Interfacial Engineering, *ACS Nano*, 2019, **13**(10), 11874–11881.

9 Y. W. Cheng, J. H. Dai, Y. M. Zhang, *et al.*, Transition metal modification and carbon vacancy promoted Cr_2CO_2 (MXenes): a new opportunity for a highly active catalyst for the hydrogen evolution reaction, *J. Mater. Chem. A*, 2018, **6**(42), 20956–20965.

10 G. Zhang, X. Li, K. Chen, *et al.*, Tandem Electrocatalytic Nitrate Reduction to Ammonia on MBene, *Angew. Chem., Int. Ed.*, 2023, **62**(13), 202300054.

11 Y. P. Zhu, T. Z. Ren and Z. Y. Yuan, Mesoporous Phosphorus-Doped g-C_3N_4 Nanostructured Flowers with Superior Photocatalytic Hydrogen Evolution Uerformanc, *ACS Appl. Mater. Interfaces*, 2015, **7**(30), 16850–16856.

12 Y. An, S. Gong, Y. Hou, *et al.*, MoB_2: A New Multifunctional Transition Metal Diboride Monolayer, *J. Phys.: Condens. Matter*, 2019, **32**(5), 055503.

13 J. Wang, M. Khazaei, M. Arai, *et al.*, Semimetallic Two-dimensional TiB_2: Improved Stability and Electronic Properties Tunable by Biaxial Strain, *Chem. Mater.*, 2017, **29**(14), 5922–5930.

14 J. Wang, T. N. Ye, Y. Gong, *et al.*, Discovery of Hexagonal Ternary Phase Ti_2InB_2 and its Evolution to Layered Boride TiB, *Nat. Commun.*, 2019, **10**(1), 2284.

15 T. F. Jaramillo, K. P. Jørgensen, J. Bonde, *et al.*, Identification of active edge sites for electrochemical H_2 evolution from MoS_2 nanocatalysts, *Science*, 2007, **317**(5834), 100–102.

16 N. Miao, Y. Gong, H. Zhang, *et al.*, Discovery of Two-dimensional Hexagonal MBene HfBO and Exploration on its Potential for Lithium-Ion Storage, *Angew. Chem., Int. Ed.*, 2023, **135**(36), 202308436.

17 B. Li, Y. Wu, N. Li, *et al.*, Single-Metal Atoms Supported on MBenes for Robust Electrochemical Hydrogen Evolution, *ACS Appl. Mater. Interfaces*, 2020, **12**(8), 9261–9267.

18 T. Zhang, B. Zhang, Q. Peng, *et al.*, Mo_2B_2 MBene-Supported Single-Atom Catalysts as Bifunctional HER/OER and OER/ORR Electrocatalysts, *J. Mater. Chem. A*, 2021, **9**(1), 433–441; P. Hohenberg and W. Kohn, Inhomogeneous Electron Gas, *Phys. Rev. B: Condens. Matter Mater. Phys.*, 1964, **136**(3B), B864.

19 G. Kresse and J. Hafner, Ab initio molecular dynamics for open-shell transition metals, *Phys. Rev. B: Condens. Matter Mater. Phys.*, 1993, **48**, 13115–13118.

20 G. Kresse and J. Furthmüller, Efficiency of ab-initio total energy calculations for metals and semiconductors using a plane-wave basis set, *Comput. Mater. Sci.*, 1996, **6**, 15–50.

21 P. E. Blöchl, Projector augmented-wave method, *Phys. Rev. B: Condens. Matter Mater. Phys.*, 1994, **50**, 17953–17979.

22 J. P. Perdew, K. Burke and M. Ernzerhof, Generalized Gradient Approximation Made Simple, *Phys. Rev. Lett.*, 1996, **77**(18), 3865–3868.

23 S. Grimme, Semiempirical GGA-type density functional constructed with a long-range dispersion correction, *J. Comput. Chem.*, 2006, **27**, 1787–1799.

24 G. Henkelman, B. P. Uberuaga and H. Jonsson, A climbing image nudged elastic band method for finding saddle points and minimum energy paths, *J. Chem. Phys.*, 2000, **113**, 9901–9904.

25 G. J. Martyna, M. L. Klein and M. E. Tuckerman, Nosé-Hoover chains: the canonical ensemble *via* continuous dynamics, *J. Chem. Phys.*, 1992, **97**, 2635–2643.

26 J. K. Norskov, T. Bligaard, A. Logadottir, J. R. Kitchin, J. G. Chen and S. Pandelov, Trends in the exchange current for hydrogen evolution, *J. Electrochem. Soc.*, 2005, **152**, J23–J26.

27 G. P. Gao, A. P. O'Mullane and A. J. Du, 2D MXenes: A New Family of Promising Catalysts for the Hydrogen Evolution Reaction, *ACS Catal.*, 2017, 7, 494–500.

28 N. Miao, Y. Gong, H. Zhang, *et al.*, Discovery of Two-dimensional Hexagonal MBene HfBO and Exploration on its Potential for Lithium-Ion Storage, *Angew. Chem., Int. Ed.*, 2023, **135**(36), e202308436.

29 X. Lv, W. Wei, H. Wang, *et al.*, Holey graphitic carbon nitride (g-CN) supported bifunctional single atom electrocatalysts for highly efficient overall water splitting, *Appl. Catal., B*, 2020, **264**, 118521.

30 H. Niu, X. Wang, C. Shao, *et al.*, Revealing the oxygen reduction reaction activity origin of single atoms supported on gC_3N_4 monolayers: a first-principles study, *J. Mater. Chem. A*, 2020, **8**(14), 6555–6563.

31 V. G. Garcia and G. J. Inacio, Exploring the potential of α-Ge (1 1 1) monolayer in photocatalytic water splitting for hydrogen production, *FlatChem*, 2024, **48**, 100753.

32 W. P. Morais, G. J. Inacio, *et al.*, CO_2 Reduction Reactivity on the SiC Monolayer with Doped Topological Defects, *Energy Fuels*, 2025, **39**(12), 5767–5777.

33 J. Zong, C. He and W. Zhang, Ultrafast carrier recombination in a BC 6 N/SnXY Z-scheme heterostructure for water splitting: insights from ground-and excited-state carrier dynamics, *J. Mater. Chem. A*, 2024, **12**(29), 18528–18536.

34 W. Zhang, X. He and C. He, The "dp orbital hybridization"-guided design of novel two-dimensional MOFs with high anchoring and catalytic capacities in Lithium–Sulfur batteries, *J. Colloid Interface Sci.*, 2025, **678**, 540–548.